lubricants

MDPI

Article

Faster EHL FEM Simulations Based on AI-Driven Initial Guesses: Evaluation of Hybrid Modeling Approaches

Josephine Kelley [1,*], Wassim Habchi [2,3], Volker Schneider [1], Marko Tošić [4], Chongyu Zhang [4], Thomas Lohner [4] and Max Marian [1,5,*]

[1] Institute of Machine Design and Tribology (IMKT), Leibniz University Hannover, 30823 Garbsen, Germany; schneider@imkt.uni-hannover.de
[2] Department of Industrial and Mechanical Engineering, Lebanese American University, Byblos P.O. Box 36, Lebanon; wassim.habchi@lau.edu.lb
[3] PIMM Lab, Arts et Métiers Institute of Technology, 75013 Paris, France
[4] Gear Research Center (FZG), Department of Mechanical Engineering, School of Engineering and Design, Technical University of Munich, 85748 Garching, Germany; marko.tosic@tum.de (M.T.); chongyu.zhang@tum.de (C.Z.); thomas.lohner@tum.de (T.L.)
[5] Department of Mechanical and Metallurgical Engineering, School of Engineering, Pontificia Universidad Católica de Chile, Macul 6904411, Region Metropolitana, Chile
* Correspondence: kelley@imkt.uni-hannover.de (J.K.); marian@imkt.uni-hannover.de (M.M.)

Abstract

Numerical elastohydrodynamic lubrication (EHL) simulations provide physically consistent, locally resolved solutions but may require substantial nonlinear iteration effort. This study investigates a hybrid modeling approach in which artificial neural network (ANN) predictions are used as informed initial guesses for a fully coupled finite element method (FEM) solver for smooth isothermal Newtonian EHL line contacts. Different initialization strategies are compared across 58 cases with different operating conditions. This includes two conventional approaches that are based on Hertzian contact theory and employ either a constant or an analytically estimated central film thickness in initializing the rigid-body separation. Moreover, two ANN-supported initialization strategies are investigated: one based on the predicted pressure distribution, and another more comprehensive one using the predicted pressure and film thickness distributions. Performance is evaluated using the nonlinear iteration count, the dimensionless initial residual, and the dimensionless root mean square (RMS) difference from the converged solution. Both ANN-based strategies substantially improve the initial field proximity and generally accelerate convergence. The first one, using only the ANN-predicted pressure distribution in the initialization process, achieves the largest reduction in computational effort, decreasing the median iteration count and overall CPU time by approximately 55% and 61%, respectively, relative to the conventional approach that uses an analytically estimated central film thickness, which is taken as a reference. The second one, using both the ANN-predicted pressure and film thickness distribution in the initialization process, produces the lowest initial residual but achieves smaller median iteration and overall CPU time reductions of approximately 40% and 58%, respectively. The results demonstrate that transferring additional predicted distributions does not necessarily improve nonlinear convergence. The proposed hybrid approach preserves the physical consistency of the converged FEM solution while substantially reducing numerical effort.

Keywords: elastohydrodynamics; finite element method; artificial intelligence; machine learning; neural network

Check for updates

Received: 9 September 2026
Revised: 11 November 2026
Accepted: 15 November 2026
Published: 18 November 2026

Copyright: © 2026 by the authors. Licensee MDPI, Basel, Switzerland. This article is an open access article distributed under the terms and conditions of the Creative Commons Attribution (CC BY) license.

1. Introduction

Rolling bearings, gears, and other highly loaded machine elements transmit forces and torques through concentrated contacts that mostly operate under elastohydrodynamic lubrication (EHL). The lubricant viscosity varies strongly with pressure, thereby causing hydrodynamic pressure within the lubricant film to become sufficiently high to cause substantial elastic deformation of the contacting bodies. Consequently, film formation results from the nonlinear interaction of lubricant flow, solid deformation, and force equilibrium [1]. Accurate prediction of the pressure and film thickness distributions is essential for evaluating friction, the risk of surface interaction or the electrical properties in machine elements. Numerical EHL models provide detailed, locally resolved solutions and can account for physical effects that cannot be adequately represented by simplified analytical approaches. Among the established numerical strategies are multigrid and multilevel methods [2,3], finite volume method (FVM)-based approaches [4–6], as well as fully coupled finite element method (FEM) formulations [7]. In particular, full-system FEM formulations solve the governing hydrodynamic, elasticity, and load-balance equations in a strongly coupled manner and have therefore become an important tool for mechanism-oriented EHL analysis [8]. Despite recent advances in computational efficiency and the use of model order reduction (MOR) [9] to reduce per-iteration computational efforts, the nonlinear and tightly coupled character of the governing equations makes their numerical solution require numerous iterations to reach convergence. The required effort increases further for fine spatial discretization, extensive parameter studies, transient analyses, or the inclusion of non-Newtonian and thermal effects.

For practical calculations at the component or system levels, EHL conditions are therefore often approximated using analytical film thickness equations based on non-dimensional similarity parameters. These approaches are computationally efficient and can be readily integrated into bearing, gear, drivetrain, or multibody simulation environments. Their development and associated correction factors for compressibility, thermal effects, non-Newtonian behavior, starvation, and surface roughness have been reviewed comprehensively by Marian et al. [10]. Despite their practical value, analytical equations generally provide only scalar quantities, such as the central or minimum film thickness, and are subject to restrictions arising from the assumptions and parameter ranges of the numerical data used in their derivation. They do not reproduce the complete local pressure and film thickness distributions and may lose accuracy outside their validity range.

Machine learning (ML) has emerged as a potential means of reducing the traditional trade-off between numerical accuracy and computational efficiency. Applications of ML in tribology now include the prediction of lubricant-film parameters, friction, wear, and component condition, as summarized in several recent reviews [11–14]. Within EHL modeling, artificial neural networks (ANNs), Gaussian process regression, and support vector machines have been trained using data generated by numerical simulations. Marian et al. [15] demonstrated that ML models can predict central and minimum film thicknesses more accurately than established analytical equations over the investigated parameter ranges. Issa et al. [16] extended ML-based film thickness prediction to elliptical contacts using Gaussian process regression, while Tošić et al. [17] investigated ANN predictions for elliptical contacts with varying entrainment directions. Habchi and Bair [18] employed ML to characterize high-pressure lubricant piezoviscous behavior for minimum film thickness estimation, whereas Zhang et al. [19] developed a modular approach for non-Newtonian EHL film thickness prediction. Beyond these investigations, Walker et al. [20] demonstrated the applicability of ANNs to tribological performance predictions in machine elements, while Wang et al. [21] and Cartwright et al. [22] considered additional non-Newtonian and thermal effects.

Most of these studies use ML models as surrogates that replace the numerical EHL calculation. Once trained, such models can predict the quantities of interest without solving the EHL equations numerically, but their predictions remain approximations of the numerical reference solution. Their accuracy depends on the representativeness and density of the training data, the selected input representation, and the model architecture. Moreover, many surrogate models predict only scalar quantities and therefore do not provide the spatially resolved information available from numerical simulations. Kelley et al. [23] addressed this limitation by developing an ANN for the locally resolved pressure and film thickness distributions of smooth isothermal Newtonian EHL line contacts. Based on a database of almost 48k FEM simulations, the ANN reproduced the characteristic EHL distributions over a broad parameter space and enabled their rapid evaluation. Nevertheless, even highly accurate ANN predictions may exhibit local deviations, particularly near steep gradients and the pressure spike, and they do not inherently satisfy the coupled governing equations to the convergence tolerances of a numerical solver.

Beyond tribology, hybrid approaches that combine machine learning predictions with conventional numerical solvers have attracted increasing attention. Rather than replacing the numerical solver, learned solution fields are employed as informed initial guesses to accelerate iterative convergence while retaining the accuracy of the converged numerical solution. Aghili et al. [24] demonstrated this concept for nonlinear elliptic partial differential equations using Fourier neural operators, while Zhou et al. [25] investigated neural operator-based warm starts for steady-state computational fluid dynamics simulations. Very recently, Taghikhani et al. [26] extended this strategy to nonlinear finite element analysis, and Eshaghi et al. [27] and Wang et al. [28] explored related approaches for iterative solvers and finite element simulations, respectively.

Despite growing interest in ML-based predictions for EHL contacts, previous studies have primarily focused on replacing numerical EHL solvers through surrogate models. Comparatively little attention has been paid to using ML predictions to improve the convergence behavior of physically consistent EHL solvers. Such a hybrid strategy, however, can overcome the limitations of surrogate models by using an ML prediction not as the final solution, but as an informed ("artificially educated") initial guess for a conventional numerical solver; see Figure 1. The numerical method then retains responsibility for satisfying the governing equations, while the ANN places the iterative solution process closer to the converged state. This concept has recently been investigated for thermo-elastohydrodynamic point contacts. Using hybrid ANN–finite-volume frameworks, Kaliafetis et al. [29] predicted several scalar and spatially resolved quantities, including pressure and temperature distributions, which were subsequently used to initialize thermal point-contact simulations. Acceleration was primarily assessed using wall-clock computation time, and the investigation simultaneously addressed the additional challenge of estimating three-dimensional temperature distributions. The present study has a related general motivation but a deliberately different focus. It examines smooth isothermal Newtonian EHL line contacts and isolates the influence of ANN-based initialization on the nonlinear convergence behavior of a fully coupled FEM solver. Restricting the analysis to the isothermal Newtonian problem enables a detailed examination of the hydrodynamic–elastic coupling without superimposing the substantially different convergence behavior associated with thermal equations and their associated higher-dimensional temperature distributions. Furthermore, solver acceleration is evaluated through hardware-independent numerical criteria rather than relying solely on wall-clock time. The principal metric is the number of nonlinear iterations required to reach convergence. This is complemented by the development of the global residual and by the L_2-norm of the difference from the converged solution during the iterative process. These measures reveal not only whether an initialization strategy reduces computational

effort, but also how closely it places the solver to the final solution and how it affects the subsequent convergence trajectory.

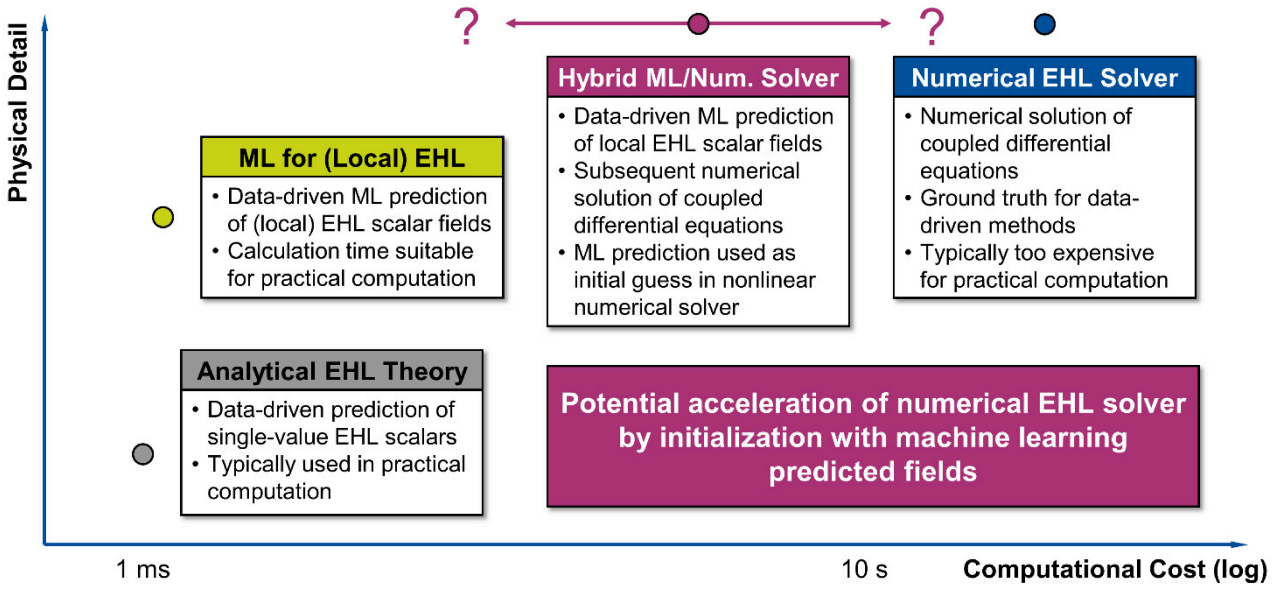


Figure 1. Physical detail versus computational cost of analytical EHL theory, conventional numerical EHL solvers, ML approach for EHL prediction as well as a hybrid modeling approach using a numerical solver with ML-driven initialization.

While Kaliafetis et al. [29] demonstrated substantial computational acceleration through ANN-supported initialization of more complex TEHL point-contact simulations, the relationship between the quality and consistency amongst the different predicted initial fields and the subsequent nonlinear convergence behavior remains less thoroughly understood. The present study addresses this complementary question using a fully coupled FEM formulation for isothermal Newtonian EHL line contacts. By comparing different initialization strategies and evaluating their initial residuals, deviations from the converged solution, and subsequent convergence trajectories, the investigation seeks to identify which ANN-predicted quantities contribute most effectively to nonlinear solver convergence. Particular attention is given to whether increasing the amount of predicted information in the initial guess necessarily improves convergence, or whether a more selective initialization can achieve greater numerical efficiency.

For this purpose, the locally resolved ANN developed by Kelley et al. [23] is coupled with a fully coupled FEM solver. Two ANN-supported initialization strategies are compared with conventional approaches: one using the predicted pressure distribution only and another incorporating both pressure and film thickness distributions. Their influence on nonlinear convergence is systematically evaluated across representative operating conditions using iteration counts, residual evolution, and deviations from the converged solution. The results provide insights into the effectiveness and limitations of ANN-driven initialization for EHL simulations.

2. Theory and Methods

2.1. Governing Equations for the Isothermal EHL Line Contact Model

Following the original data originating from Kelley et al. [23], the present study considers an isothermal, fully flooded, steady-state EHL line contact between two smooth surfaces. The geometry was assumed to be invariant in the direction transverse to rolling, so that the

hydrodynamic problem can be formulated along the rolling direction x. The two contacting bodies were represented by an equivalent elastic solid with reduced Young's modulus

$$\frac{2}{E'} = \frac{1-\nu_1^2}{E_1} + \frac{1-\nu_2^2}{E_2}, \tag{1}$$

where E_1, E_2, ν_1, and ν_2 are the Young's moduli and Poisson's ratios of the two bodies, respectively. The undeformed gap was described by the equivalent radius of curvature R, and the contact was subjected to the normal line load per unit length F_N. The lubricant flow was described using the steady-state Reynolds equation for a compressible, piezoviscous lubricant

$$\frac{\partial}{\partial x}\left(\frac{\rho h^3}{12\eta}\frac{\partial p}{\partial x}\right) = u_{ent}\left(\frac{\partial \rho h}{\partial x}\right), \tag{2}$$

where p is the hydrodynamic pressure, h is the lubricant film thickness, η is the pressure-dependent dynamic viscosity, ρ is the pressure-dependent lubricant density, and u_{ent} is the entrainment velocity. The lubricant viscosity was modeled using the Roelands pressure–viscosity relation [30], while the lubricant density was represented by the Dowson–Higginson pressure-dependent relationship [31]. These comparatively simple constitutive descriptions were retained to maintain consistency with the numerical dataset developed in the preceding study [23]. Cavitation was represented by imposing non-negative pressure via a penalty term and an ambient-pressure outlet condition. For the fully flooded, isothermal EHL conditions considered here, the choice of cavitation treatment is not expected to substantially affect the pressure and film thickness distributions or the relative convergence benefits of ANN-based initialization, as cavitation is primarily confined to the outlet region. Mass-conserving cavitation formulations become particularly relevant when considering more complex lubrication conditions such as multiple consecutive contacts with film break-up and re-formation or micro-EHL within mixed lubricated contacts. Nevertheless, differences in the numerical formulation may influence solver convergence and would require separate investigation.

The Reynolds equation was coupled to the elastic deformation of the contacting bodies and to the global load-balance condition

$$\int_{\Omega_c} p \, dx = F_N, \tag{3}$$

where Ω_c denotes the hydrodynamic computational domain.

As illustrated in Figure 2, the local film thickness

$$h = h_0 + \frac{x^2}{2R} - u_z, \tag{4}$$

was obtained from the undeformed parabolic geometry, the rigid-body separation h_0 (which, except for very lightly loaded contacts, typically takes a negative value, indicating interpenetration of the undeformed bodies), and the normal elastic deformation at the surface u_z. Thereby, except for very lightly loaded contacts, h_0 typically takes a negative value, indicating interpenetration of the undeformed bodies, and u_z is also negative, given that the equivalent solid body is subjected to a pressure load over the Reynolds domain (see Figure 3) in the negative z-direction. The elastic deformation of the equivalent solid under the influence of the applied pressure load was calculated by solving the steady-state linear elasticity equation

$$\nabla[C{\cdot}\varepsilon(U_d)] = 0. \tag{5}$$

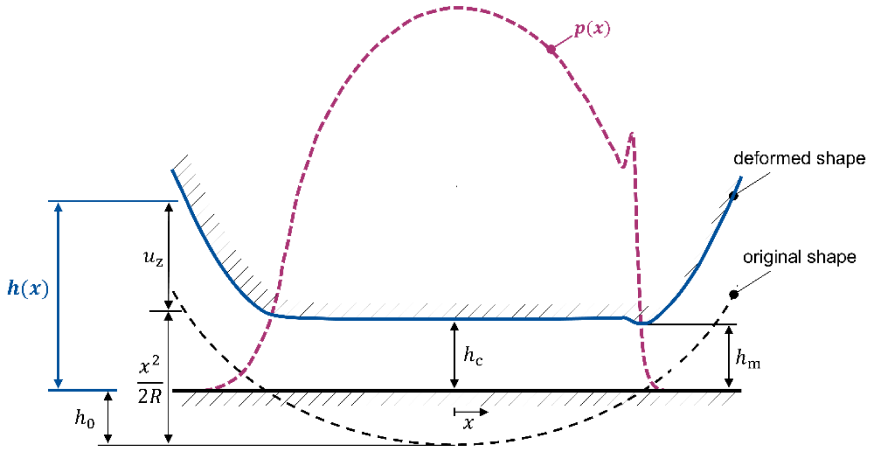


Figure 2. EHL pressure and film thickness distribution, with the film thickness being composed of the undeformed parabolic geometry, the rigid body separation, and the elastic deformation.

Thereby, C is the generalized Hooke's-law elasticity matrix, ε is the contracted infinitesimal strain tensor, and U_d is the displacement vector. The surface deformation entering the film thickness equation was given by the normal component of the displacement vector.

The present contribution was intentionally restricted to Newtonian and isothermal conditions. It therefore isolates the influence of the initial pressure and elastic deformation distributions on the nonlinear hydrodynamic–elastic solution process without introducing the additional equations and convergence characteristics associated with non-Newtonian or thermal transport effects.

2.2. Non-Dimensional Formulation

To improve numerical conditioning and to provide a generalized representation of the investigated EHL conditions, the governing equations were solved in non-dimensional form. To this end, the relevant variables were normalized by the Hertzian (subscript H) or reference ambient values (subscript 0):

$$X = \frac{x}{b_H},\ P = \frac{p}{p_H},\ H = \frac{h \cdot R}{b_H^2},\ U_z = \frac{u_z \cdot R}{b_H^2},\ \overline{\eta} = \frac{\eta}{\eta_0},\ \overline{\rho} = \frac{\rho}{\rho_0}. \tag{6}$$

The same normalization was applied to the ANN outputs and to the corresponding FEM variables. This ensured a consistent transfer of the locally resolved ANN predictions to the FEM discretization.

The operating conditions, contact geometry, and material and lubricant properties were further characterized by the conventional Dowson–Higginson dimensionless parameters [32,33]. The dimensionless speed parameter U, load parameter W, and material parameter G are defined as

$$U = \frac{\eta_0 \cdot u_{ent}}{E' \cdot R}, W = \frac{F_N}{E' \cdot R}, G = \alpha_p \cdot E', \tag{7}$$

where η_0 is the lubricant viscosity at ambient pressure and α_p is the pressure–viscosity coefficient. For the definition and visualization of the investigated parameter space, the Blok and Moes load parameter M and material parameter L were used [34,35]:

$$M = W \cdot (2 \cdot U)^{-\frac{1}{2}}, L = G \cdot (2 \cdot U)^{\frac{1}{4}}. \tag{8}$$

2.3. FEM-Based EHL Solver

The non-dimensional governing equations were discretized using the fully coupled finite element formulation introduced by Habchi et al. [7,36]. Thereby, the Reynolds equa-

tion, the elasticity equation, and the load-balance condition were assembled into a single coupled nonlinear system

$$R(q) = 0, \tag{9}$$

where q contains the discrete lubricant-pressure distribution, the elastic displacement degrees of freedom, and the rigid-body separation. Solving the equations in a fully coupled manner avoids an external iterative exchange between the hydrodynamic and elastic subproblems and directly accounts for their strong mutual coupling. As shown in Figure 3, the Reynolds equation was discretized along the one-dimensional hydrodynamic domain, whereas the deformation of the equivalent elastic body was evaluated on a two-dimensional rectangular domain. All parametric studies employed the same standard finite element mesh configuration, following Habchi [7], with local refinement in and around the Hertzian contact region to adequately resolve the pronounced pressure gradients and outlet-side film thickness constriction. The "normal" mesh case with a total of 249 quadratic elements (499 nodes) within the 1D hydrodynamic domain and 2562 quadratic triangular elements (5419 nodes) within the 2D elastic solid domain was employed, guaranteeing grid-independent solutions. At the inlet and outlet boundaries of the Reynolds domain, the lubricant pressure was prescribed at ambient pressure. The Reynolds computational domain extended sufficiently far into the inlet and outlet regions to minimize the influence of the hydrodynamic boundary conditions on the pressure and film thickness distributions. On the upper boundary of the elastic domain, the hydrodynamic pressure acted as a distributed normal stress over the Reynolds domain, while the remaining part of the upper surface was stress-free. The lower boundary of the elastic domain was fixed to suppress rigid-body motion and to approximate the decay of the elastic displacement at sufficiently large distance from the contact, thereby justifying the assumption of an elastic half-space in the vicinity of the contact region. On the lateral boundaries, the displacement normal to the respective boundaries was constrained, whereas tangential displacement remained unrestricted. Static Condensation with Splitting (SCS) [11] was used as a MOR technique to get rid of the unnecessary elastic degrees of freedom (i.e., the tangential component of the elastic deformation field inside the Reynolds domain, as well as the entire field outside of it), and only retain the needed ones (i.e., the normal component of the elastic deformation field inside the Reynolds domain). Only the latter is needed for defining the geometry of the lubricating film, see Equation (4). Therefore, the linear elasticity part is formulated as a function of $U_Z(X)$ over the 1D Reynolds domain, instead of U over the entire 2D computational domain of the equivalent solid, reducing the overall dimension of the problem to 1D and allowing substantial savings in computational effort.

The resulting nonlinear algebraic system was solved iteratively following Habchi [7]. The sparse linearized system of equations arising at every iteration was solved using UMFPACK [37], a direct sparse linear solver. At each nonlinear iteration k, the current solution vector $q^{(k)}$ was updated based on the assembled residual and the corresponding linearized system. Convergence was assessed using the global residual of the coupled equations. The dimensionless convergence criterion for the global residual was set at 10^{-6}, in accordance with [7]. The same nonlinear solution procedure, finite element mesh, numerical stabilization, and convergence criterion were applied to all calculations considered in this study in accordance with [7].

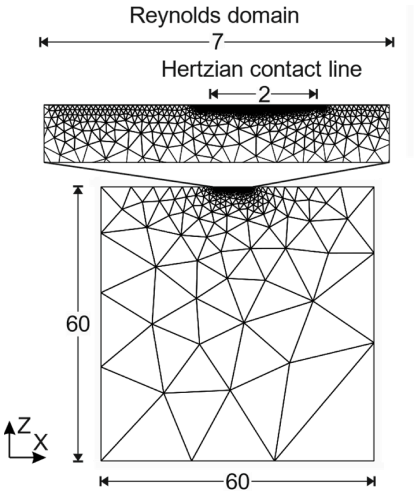


Figure 3. Two-dimensional computational domain with finite element mesh as well as a zoom-in view of the refined, one-dimensional Reynolds domain on top, including dimensionless length scales.

The different initialization strategies described in Sections 2.4 and 2.5, did not modify the governing equations, the finite element formulation, nor the final convergence requirement. They only provided alternative initial values for selected components of $q^{(0)}$. Irrespective of the initialization strategy, the FEM solver remained responsible for enforcing the Reynolds equation, elastic equilibrium, and force balance to the prescribed numerical tolerance. The converged FEM solution was consequently the same for all investigated initialization strategies, within prescribed convergence tolerances, and has previously been verified and validated extensively [7]. Differences between the strategies were instead evaluated through the nonlinear iteration count, the residual evolution, and the distance between the initial and converged solution fields, as described in Section 2.7.

2.4. Hybrid ANN-FEM Framework

The hybrid framework combined the locally resolved ANN prediction developed by Kelley et al. [23] with the fully coupled FEM solver described in Section 2.3. In contrast to a conventional surrogate-model application, the ANN prediction was not regarded as the final EHL solution. Instead, it was used to initialize selected variables of the nonlinear FEM system. The FEM solver subsequently corrected the predicted fields and iterated until the same convergence criterion as in the conventional FEM calculations was fulfilled. Thus, the ANN supplied an informed starting point, while the converged solution continued to satisfy the Reynolds equation, elastic equilibrium, and normal-force balance within the prescribed numerical tolerance.

The ANN was based on the same database of 47,952 isothermal EHL line contact simulations used in [23]. Each operating condition was represented by six input parameters, namely the normal force per length unit F_N, the entrainment speed u_{ent}, the equivalent cylinder radius R, the equivalent elastic modulus E', the dynamic viscosity at ambient conditions η_0, and the pressure–viscosity coefficient α_p. The output layer contained 202 neurons, corresponding to the dimensionless pressure and film thickness distributions at 101 uniformly spaced positions in the interval $-2.0 \leq X \leq 1.2$. The fully connected feed-forward network comprised two hidden layers with 32 neurons each and a total of 9002 trainable parameters. Hyperbolic tangent activation functions were applied in the hidden layers, while the output layer was linear. The architecture and preprocessing procedure were retained from [23]. Thereby, the ANN architecture and its predictive performance were previously investigated in detail and 60% of the dataset was used for training and 40% for independent testing, yielding a testing error of 1.54×10^{-4}. Since the present work did not aim to reassess the

ANN as an independent surrogate model, the network was retrained using the complete available dataset. This allowed all FEM solutions to contribute to the determination of the network weights and was intended to provide the most accurate possible initial fields within the considered parameter space. The architecture, normalization, and optimization procedure remained unchanged compared to [23], with a jointly calculated mean squared error (MSE) loss function and a convergence tolerance of 10^{-4}. Due to stagnated convergence of the Adam optimizer, a learning rate of 10^{-5} was used and the momentum coefficient was reduced from 0.9 to 0.8. The retrained network reached a final training error of 1.905×10^{-4}.

A Python-based (version 3.14.4) coupling routine evaluated the ANN for the dimensional input parameters of the queried operating condition. The predicted dimensionless pressure and film thickness distributions were initially available at the 101 spatial positions used for ANN training. Since these positions did not generally coincide with the nodes of the refined FEM mesh, the predicted distributions were transferred to the FEM discretization by linear spline interpolation. The latter was selected for its simplicity and robustness, particularly in the presence of steep pressure gradients and localized pressure spikes. Unlike unconstrained higher-order interpolation methods, it does not introduce additional extrema between the predicted spatial points. Potential minor negative values in the pressure data present in the ANN prediction and resulting interpolation were replaced by a lower limiting value of 10^{-9} to avoid unphysical initial pressure or film thickness values. The interpolated ANN distributions were subsequently assigned to the corresponding components of the initial FEM solution vector $q^{(0)}$. The coupling procedure, therefore, modified only the initial state of the nonlinear solution process. It did not alter the FEM mesh, governing equations, constitutive relationships, numerical stabilization, boundary conditions, nor convergence tolerance. The hybrid and conventional calculations consequently converged toward the same numerical EHL solution within prescribed convergence tolerances, whereas their convergence paths and required numbers of nonlinear iterations could differ.

2.5. Initialization Strategies

Four initialization strategies were included in the comparison; see Figure 4. Two represented conventional FEM procedures based on a Hertzian initial pressure distribution, while the other two used locally resolved ANN predictions within the hybrid framework described in Section 2.4. The governing equations and nonlinear solution procedure were identical in all cases.

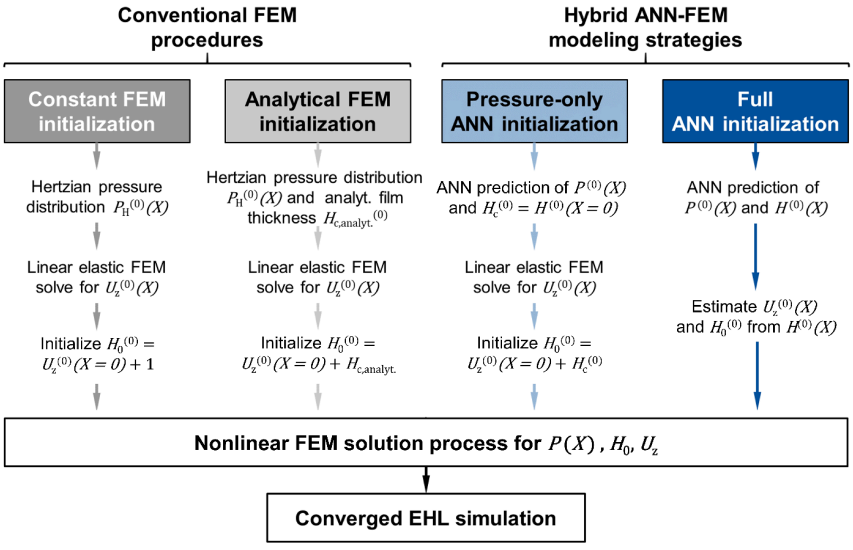


Figure 4. Conventional and hybrid modeling initialization strategies selected for comparison.

The first conventional strategy for the non-hybrid, standard FEM-approach used the Hertzian pressure distribution as the initial pressure field $P^{(0)}$, along with its FEM-computed corresponding solid elastic deformation field as $U^{(0)}$, and prescribed a constant dimensionless initial central film thickness of

$$H_{\mathrm{c,const.FEMinitialization}} = 1, \tag{10}$$

allowing us to set the initial rigid-body separation ${H_0}^{(0)}$ from an inversion of Equation (4), applied at the contact center ($X = 0$). This strategy required no preceding estimation of the film thickness and provided a simple, robust initialization over the considered parameter range. It is denoted as the "constant FEM initialization" in the following.

The second conventional strategy only differed from the first one in that the initial central film thickness was estimated using an analytical central film thickness equation according to Pan and Hamrock [38]:

$$H_{\mathrm{c,analyt.FEMinitialization}} = \underbrace{2.922 \cdot U^{0.692} \cdot G^{0.47} \cdot W^{-0.166}}_{\mathrm{dimensionlessfilmthickness}} \cdot \underbrace{R \cdot \frac{R}{b_{\mathrm{H}}^2}}_{\mathrm{normalization}}. \tag{11}$$

Thereby, the first multiplication with the radius R was used to dimensionalize the film thickness according to [38], while the second multiplication with R and division by the square of the Hertzian contact half-width b_{H} was used to non-dimensionalize in accordance with the formulation described in Section 2.2. In contrast to the constant initialization, this approach accounts for the operating condition through the dimensionless speed U, material G, and load parameter W. Nevertheless, it supplied only a scalar film thickness estimate at the contact center and did not represent the locally varying film shape. This strategy is denoted as "analytical FEM initialization" in the following.

For the first hybrid strategy, the Hertzian pressure assumption was replaced by the locally resolved ANN prediction of the EHL pressure field

$$P^{(0)}(X) = P_{\mathrm{ANN}}(X), \tag{12}$$

interpolated onto the FEM mesh, and its corresponding FEM-computed elastic deformation field was used as $U_{\mathrm{Z}}^{(0)}$, while the central film thickness predicted by the ANN was used to estimate the initial rigid-body separation ${H_0}^{(0)}$ by inverting the film thickness Equation (4) as previously described. The initial local film thickness distribution was therefore not taken directly from the ANN prediction, but was reconstructed within the FEM formulation from the constant separation, the undeformed geometry, and the initialized elastic deformation. This strategy, therefore, isolated the effect of providing the nonlinear solver with a pressure field that already reproduced the principal features of the expected EHL pressure distribution, including its non-Hertzian shape and pressure-spike region, while supplying only an informed scalar estimate of the overall surface separation, and retaining the conventional treatment of the initial deformation field. Although the predicted pressure distribution was generally closer to the converged EHL pressure than the Hertzian distribution, it did not necessarily satisfy the load balance or correspond exactly to the initially prescribed film thickness and elastic deformation. The fully coupled FEM solver was therefore required to establish consistency between the initialized pressure distribution and the remaining solution variables. This strategy is denoted as the "pressure-only ANN initialization".

The second hybrid strategy used both locally resolved ANN output fields:

$$P^{(0)}(X) = P_{\mathrm{ANN}}(X), \tag{13}$$

$$H^{(0)}(X) = H_{\mathrm{ANN}}(X). \tag{14}$$

The ANN-predicted pressure and film thickness distributions were interpolated onto the FEM mesh and used to initialize the corresponding components of the nonlinear solution vector. This required the deformation component to be estimated from the ANN-predicted film thickness, as the latter did not distinguish between the contributions of H_0 and $U_Z^{(0)}$ according to Equation (4). Specifically, the magnitude of $U_Z^{(0)}(X = 0)$ must therefore be estimated. It was assumed that, for points distant from the contact center, this value may be approximated by the dimensionless deformation resulting from the Hertzian pressure distribution. Beyond being a reasonable approximation to separate the two constants $U_Z^{(0)}(X = 0)$ and H_0, the dimensionless Hertzian pressure deformation is conveniently already available (see Figure 3) and is constant across calculation conditions when computing in dimensionless form. Thus, the ANN vector entry that was most distant from the contact center ($X = -4.5$) was selected and the assumption for $U_Z^{(0)}(X = -4.5)$ was applied with a hard-coded value of $U_Z^{\mathrm{Hertz}}(X = -4.5)$, taken from the FEM solution of the Hertzian pressure problem:

$$U_Z^{(0)}(X = -4.5) \approx U_Z^{\mathrm{Hertz}}(X = -4.5) \approx -1.614. \tag{15}$$

This allowed the local values of $U_Z^{(0)}(X)$ as well as $H_0^{(0)}$ to be estimated via

$$\begin{aligned} H_0^{(0)} &= \left(H_{\mathrm{ANN}}(X) - \tfrac{X^2}{2} + U_Z^{\mathrm{Hertz}}(X) \right)\Big|_{X=-4.5} \\ U_Z^{(0)}(X) &\approx -H_{\mathrm{ANN}}(X) + \tfrac{X^2}{2} + H_0^{(0)}, \end{aligned} \tag{16}$$

Compared with the pressure-only strategy, this provided a more complete approximation of the coupled EHL state because both principal local solution fields were supplied. Nevertheless, the ANN output also did not exactly satisfy the discretized governing equations due to the finite ANN approximation error, the transfer between the ANN and FEM discretizations, the approximation of $H_0^{(0)}$ based on Hertzian contact theory, and the absence of explicit enforcement of the Reynolds equation, elasticity equation, and force balance during ANN training. The ANN distributions were therefore corrected during the subsequent FEM iterations. This strategy is denoted as the "full ANN initialization".

These initialization strategies were chosen to enable a meaningful stepwise comparison. The "constant FEM initialization" represents a commonly used and deliberately robust starting procedure that does not require any prior estimate of the EHL film thickness. It therefore serves as the practical baseline for the nonlinear solver. By contrast, the "analytical FEM initialization" already incorporates information about the operating condition through the dimensionless speed, material, and load parameters. Since this more informed estimate is expected to place the solver closer to the converged solution than the constant initialization, it provides a stricter and more appropriate benchmark for assessing the actual benefit of the ANN-supported approaches. A comparison solely against the constant initialization could otherwise overestimate the apparent acceleration achieved by the hybrid framework. The comparison between the two hybrid strategies is likewise physically and numerically meaningful. The "pressure-only ANN initialization" examines the benefit obtained from replacing the conventional Hertzian pressure assumption and from providing an ANN-based estimate of the rigid-body separation, while retaining the conventional initialization of the local elastic deformation. The "full ANN initialization" additionally reconstructs the initial deformation field from the predicted film thickness profile. Thus, comparing these two variants isolates the additional convergence benefit associated with transferring the locally resolved film thickness information into the elastic part of the coupled FEM system. The four strategies consequently form a progressive hierarchy of increasingly informed initial states, ranging from a generic conventional estimate to a locally resolved ANN-based approximation of the coupled EHL solution.

In order to quantify the effect of initialization strategy on calculation time and provide a detailed breakdown, a computational study was performed; an Intel(R) Core(TM) i5-8400H CPU (2.50 GHz) was used. The median computational times were measured based on calculations with five different operating conditions; the first five cases of Table A1 were selected. This was deemed a large enough number to arrive at a statistically robust measurement. Though the operating conditions were varied, these calculations may be considered repetitions in the context of this profiling study. From the results shown in Figure 5 it is clear that the main factors contributing to computational cost for this mesh size are the linear elastic FEM solve (when applicable) and the interpolation(s) of the ANN output to the FEM mesh (when applicable). Only the Full ANN initialization strategy avoids the linear elastic FEM solve, but instead requires two interpolations of the ANN output to the FEM mesh, as compared to the single interpolation required for the pressure-only strategy. Even so, the most computationally expensive initialization strategy (pressure-only hybrid solver) required well below 1 s, and the additional computational time due to interpolation is likely not noticeable in practice. The evaluation of the analytical models, as well as the ANN, requires almost no computational resources; though the ANN evaluation is more complex and takes more time, both are still below 1 ms, which is typically not considered a meaningful contribution. In summary, though the initialization procedures vary measurably in their computational complexity, a noticeable difference was not observed for this mesh size. The influence of the differing computational times between the initialization strategies may be disregarded when comparing the methods in the following benchmarking study.

2.6. Benchmarking Parameter Space

To systematically evaluate the convergence behavior of the four initialization strategies, a benchmarking parameter space covering different operating conditions was defined. The sampling was designed to vary the principal roller radius, load, and speed conditions while limiting the influence of additional material parameters. At the same time, the investigated cases were restricted to a region in which the ANN developed by Kelley et al. [23] had previously shown favorable predictive accuracy. The objective was not to determine the global applicability limits of the ANN, but to assess the potential convergence benefit of ANN-supported initialization when sufficiently representative pressure and film thickness predictions are available. The operating conditions were characterized using the Blok and Moes parameters M and L introduced in Section 2.2. To reduce the dimensionality of the parameter study, the equivalent elastic modulus, lubricant viscosity at ambient pressure, Roelands viscosity parameter, and pressure–viscosity coefficient were held constant at 221 GPa, 0.09 Pa·s, 0.45, and 1.56×10^{-8} Pa^{-1}, respectively. The remaining physical parameters were determined by systematically varying M, L, and R within a full factorial sampling, while filtering out physically non-meaningful EHL conditions or those falling outside the dimensional parameter ranges covered by the ANN. This resulted in a total of 58 combinations of operating conditions included in the benchmarking study, which are summarized in Table A1 and visualized in Figure 6. It is important to note that these parameter combinations were not contained in the initial training dataset of the ANN, but represent new and unseen combinations. The 58 benchmark operating conditions were each evaluated using four initialization strategies, resulting in 232 numerical evaluations. In combination with the three complementary convergence metrics, this provides a systematic basis for comparing the initialization strategies while maintaining identical numerical settings. The investigated parameter space was deliberately restricted to conditions with favorable ANN prediction accuracy, since the primary objective is to assess initialization-dependent convergence behavior rather than establish the global applicability limits of the ANN.

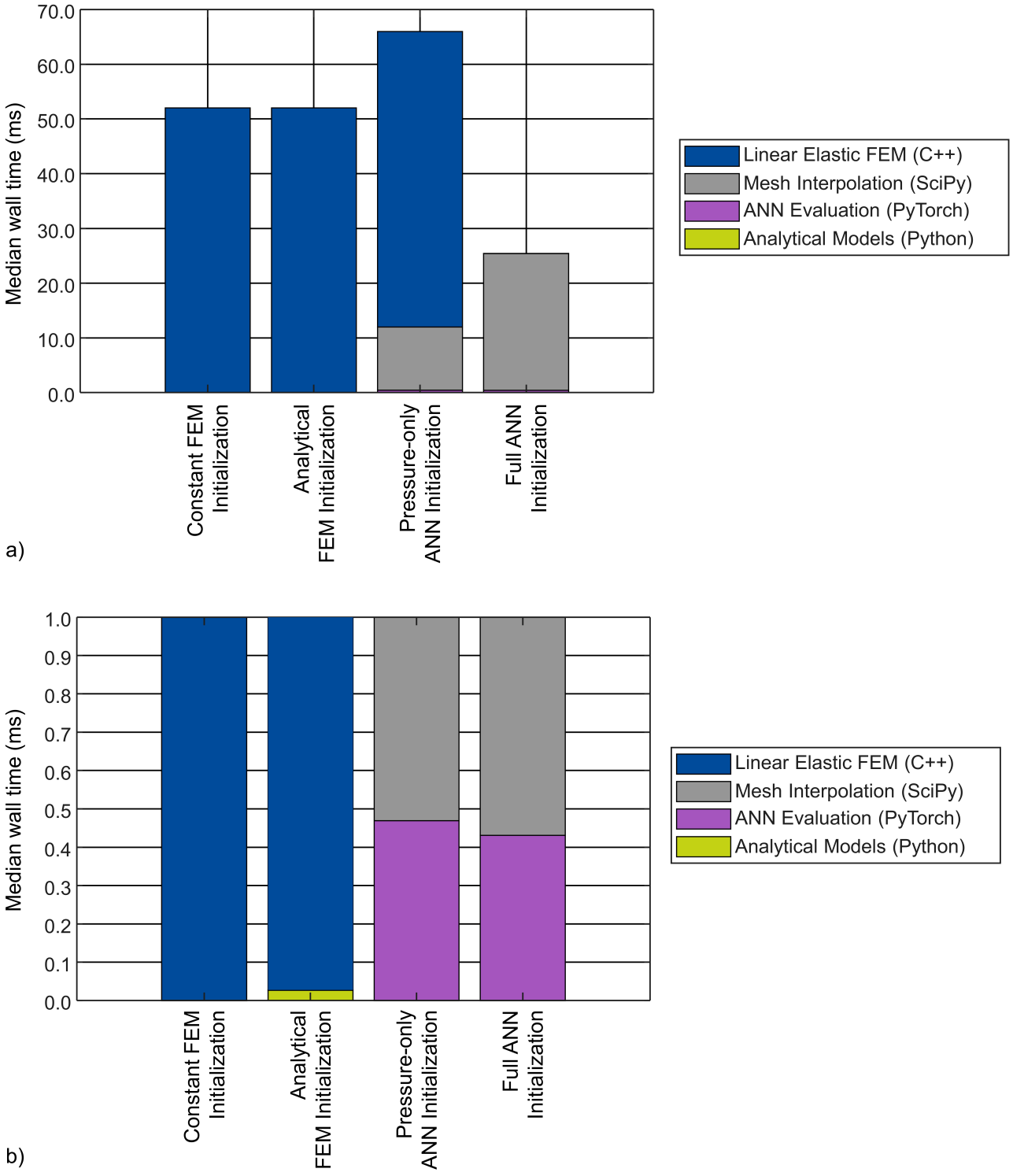


Figure 5. Breakdown of typical calculation times needed for the initialization strategies: (**a**) full calculation times; (**b**) zoomed view.

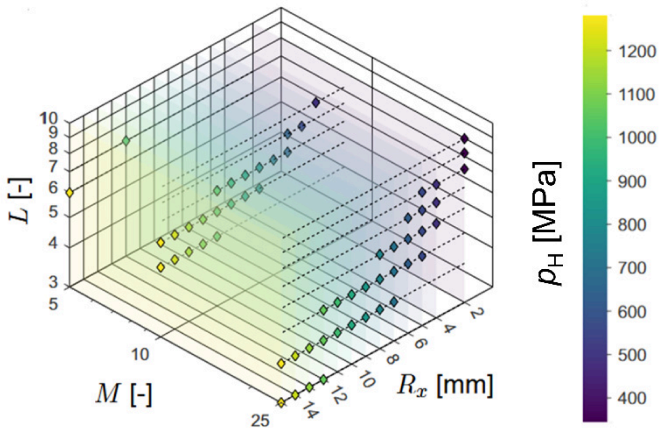


Figure 6. Three-dimensional plot of the M, L, and R parameter variations with corresponding Hertzian pressures (colored legend) considered in the benchmarking study.

2.7. Evaluation Metrics

The four initialization strategies were compared using four complementary metrics: The total number of nonlinear iterations and overall CPU time required to reach convergence, the residual of the initial solution, and a dimensionless root mean square (RMS) difference between the initial and converged solution fields. These quantities were selected to distinguish between the numerical effort required by a given initialization, the physical consistency of the initialized state, and its geometric proximity to the final solution.

The total number of nonlinear iterations and overall CPU time required to satisfy the prescribed convergence criterion were used as principal measures of solver acceleration. Both provide complementary information about the impact of the employed initialization strategies on the overall resolution process. The total number of iterations depicts the convergence trajectory for each initialization strategy, highlighting the suitability of the employed initial guess as a starting point for the overall resolution process. This information is complemented and confirmed by the residual of the initial solution as well as the dimensionless root mean square (RMS) difference between the initial and converged solution fields. The overall CPU time remains important to consider, however, since the CPU time per nonlinear iteration may exhibit significant variations. This is due to the underlying convergence trajectory within the overall nonlinear solution process and the specifics of the damped Newton procedure [7]. More specifically, if the damped Newton procedure immediately accepts a step, less wall time is needed for the corresponding nonlinear iteration since only one linear solve is required. If, however, the step cannot be immediately accepted, a damping factor is computed through an iterative procedure until an optimal value is reached that minimizes the convergence trajectory. The iterative procedure computes the damping factor based on the results (error estimates) of consecutive linear solves that involve the same Jacobian, but a different right-hand-side [7]. Therefore, the expensive LU factorization of the Jacobian is not repeated, and only the inexpensive forward- and backward-substitution steps are carried out during these sub-iterations. Hence, the increase in wall time per nonlinear iteration is not proportional to the number of sub-iterations needed to compute the optimal damping factor, since the LU factorization is only carried out at the first sub-iteration and it is not repeated at subsequent ones. This being said, it is important to consider both the iteration count as well as the overall CPU time as evaluation metrics, since they provide complementary information. The total number of nonlinear iterations is denoted as N_{it}, while the overall CPU time is denoted t_{CPU}. In addition to the iteration count and overall

CPU time, the residual of the initial guess was evaluated. For the initial FEM solution vector $q^{(0)}$, the dimensionless initial residual was defined as

$$r^{(0)} = \left\| R\left(q^{(0)}\right) \right\|_2, \tag{17}$$

where R is the assembled residual vector of the coupled Reynolds, elasticity, and load-balance equations. This quantity provides a physics-informed measure of the quality of the initial state, since it quantifies the extent to which the initialized variables violate the discretized governing equations. A smaller initial residual indicates that the initialized pressure, deformation, rigid-body separation, and force balance are already more mutually consistent, whereas a larger value indicates that more substantial nonlinear correction is required.

The geometric proximity of the initial guess to the converged FEM solution was additionally quantified using a dimensionless RMS difference. For a discrete field y, this was defined as

$$\varepsilon_{\mathrm{RMS}} = \frac{\sqrt{\frac{1}{n}\sum_{i=1}^{n}\left(y_i^{(0)} - y_i^{*}\right)^2}}{\sqrt{\frac{1}{n}\sum_{i=1}^{n}\left(y_i^{*}\right)^2}}, \tag{18}$$

where $y_{\mathrm{i}}{}^{(0)}$ denotes the initial value, $y_{\mathrm{i}}{}^{*}$ the corresponding converged FEM value, and n the number of discrete evaluation points. Since the factors $1/n$ cancel out, this dimensionless RMS difference is equivalent to a normalized L_2-norm:

$$\varepsilon_{L_2} = \frac{\left\| y^{(0)} - y^{*} \right\|_2}{\left\| y^{*} \right\|_2}. \tag{19}$$

In contrast to the initial residual, the dimensionless RMS difference or L_2-norm is a purely field-based distance measure. It quantifies how closely the initialized pressure or solid elastic deformation distribution resembles the final converged solution, but does not account for whether or not the initialized variables satisfy the governing equations. An initialization may therefore exhibit a comparatively small RMS difference while still producing a large initial residual if the fields are not mutually consistent or if local deviations occur in regions that strongly influence the nonlinear system.

Overall, the three metrics consequently describe different aspects of initialization quality. The total iteration count quantifies the numerical effort, the initial residual characterizes the physical consistency of the initial state, and the dimensionless RMS difference measures its proximity to the converged solution fields.

3. Results

The initial pressure and film thickness distributions generated by the four strategies for a representative operating condition ($M = 25$, $L = 6$, Nr. 36 in Table A1), together with the corresponding converged distributions, are displayed in Figure 7. Both conventional strategies start from the Hertzian pressure distribution. The constant FEM initialization additionally assumes a dimensionless central film thickness of one, whereas the analytical FEM initialization provides an operating-condition-dependent estimate of the central film thickness and therefore places the initial film thickness level closer to the converged solution. The pressure-only ANN initialization already reproduces the principal non-Hertzian features of the final pressure distribution and uses the ANN-predicted central film thickness to determine the initial rigid-body separation, while the local film thickness distribution is reconstructed within the FEM formulation. The full ANN initialization additionally transfers the locally resolved film thickness information and consequently provides the closest combined approximation of the converged pressure and film thickness distributions. Despite these pronounced differences in the initial states, all four strategies converge to

the same final EHL solution within the prescribed numerical tolerance. Interestingly, the pressure-only and full ANN initializations require the same number of nonlinear iterations for this representative case, although the full ANN initialization yields both a lower initial residual and a substantially smaller RMS difference to the converged solution. Conversely, the two conventional initializations differ considerably in their initial-state metrics while requiring 18 and 12 iterations, respectively. Thus, this representative case already indicates that residual, field proximity, and iteration count characterize complementary aspects of initialization quality.

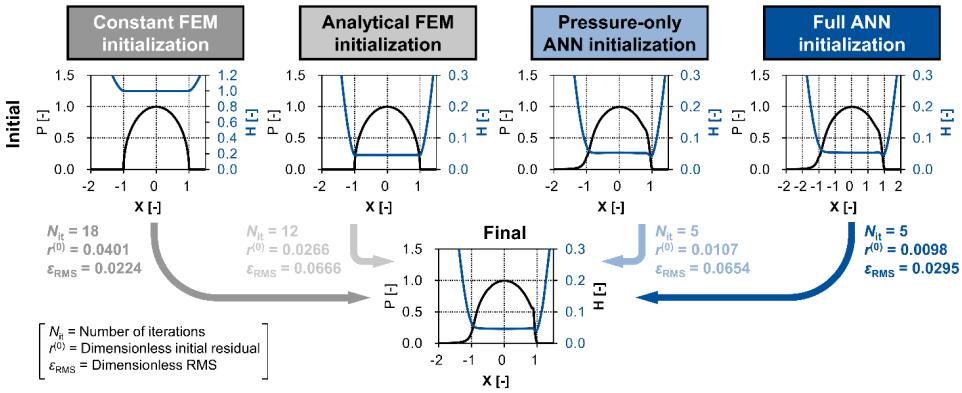


Figure 7. Initial and final pressure and film thickness distributions over contact length direction using the conventional and hybrid modeling initialization strategies for the representative operating condition case Nr. 36 ($M = 25$, $L = 6$).

The convergence behavior of the four initialization strategies over all 58 combinations of operating conditions considered in the benchmarking study is summarized in Figure 8. The box plots feature the distributions of the total number of nonlinear iterations, the overall CPU time (excluding initialization time, which was provided in Figure 5, and shown to yield minimal differences amongst the considered initialization strategies), the dimensionless initial residual, and the dimensionless RMS difference between the initialized and converged solution distributions. These absolute values are complemented in Figure 9 by presenting the percentage changes obtained with the two hybrid strategies relative to the analytical FEM initialization. The latter was selected as the reference because it represents the more informed of the two conventional initialization procedures.

As shown in Figure 8a,b, both conventional FEM initialization strategies required similar median numbers of iterations and overall CPU time, despite a notably more pronounced scatter in CPU times for the analytical initialization strategy. Their median iteration counts were approximately 15, and their median CPU times were around 300 ms. The analytical initialization therefore did not produce a systematic reduction in iteration count and CPU time relative to the robust constant initialization, despite providing an operating-condition-dependent estimate of the rigid-body separation. Moreover, the analytical strategy exhibited several high-value outliers in iteration counts, including individual calculations requiring approximately 30 to 45 iterations. This indicates that a more accurate scalar estimate of the central film thickness does not necessarily provide a correspondingly favorable initial state for the fully coupled nonlinear system. In turn, both hybrid modeling strategies substantially reduced the typical iteration count and overall CPU time. The pressure-only ANN initialization showed the lowest median value, requiring approximately 7 nonlinear iterations, while the full ANN initialization required approximately 9 iterations. Both strategies yielded a median overall CPU time of 130 ms, confirming that the overall CPU time is not necessarily proportional to the number of iterations, as discussed in Section 2.7. The interquartile ranges for iteration counts and overall CPU times of both hybrid strategies

were clearly shifted toward lower values compared with the conventional approaches. The percentage changes relative to the analytical FEM initialization are shown in the first group of Figure 9. For most operating conditions, the pressure-only ANN initialization reduced the iteration count by approximately 40–65%, with a median reduction of roughly 55%. The full ANN initialization also reduced the iteration count in most cases, with a median reduction of approximately 40%. However, its distribution was broader and contained individual cases in which the required number of iterations increased relative to the analytical FEM reference. Resulting reductions in overall CPU time had a median of roughly 61% for the pressure-only ANN initialization, and 58% for the full ANN initialization.

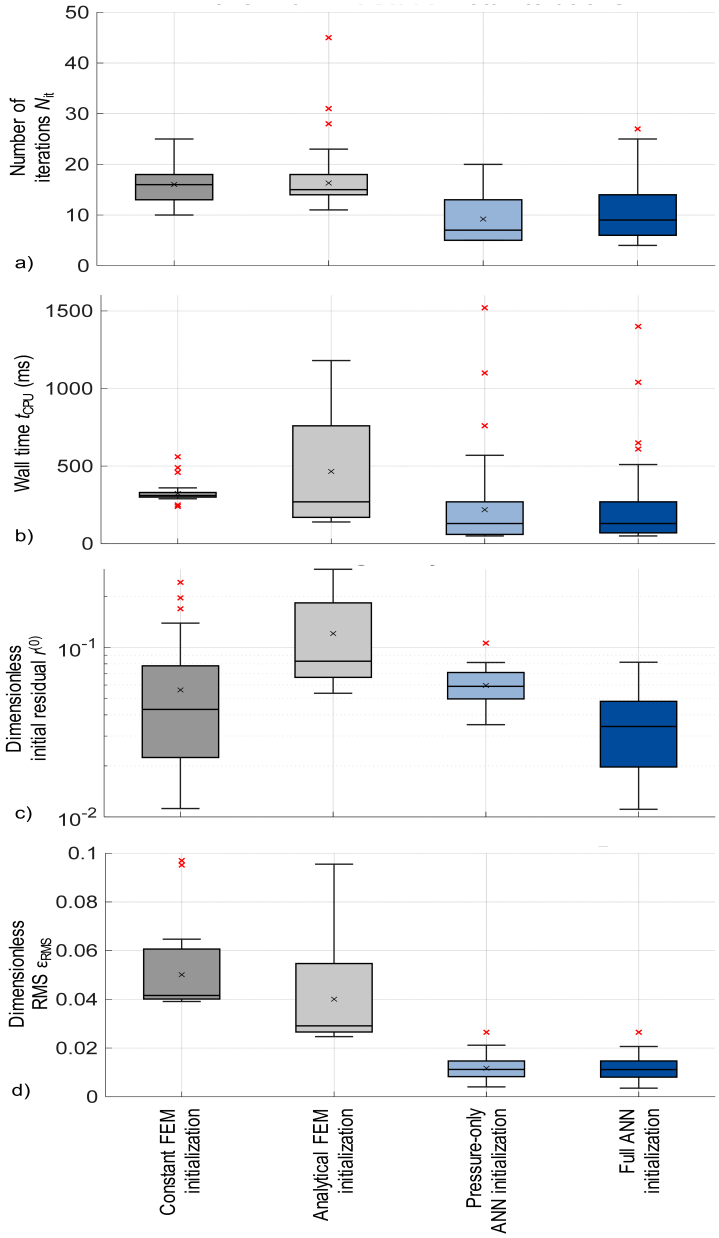


Figure 8. (**a**) Number of iterations and (**b**) overall CPU time (excluding initialization time), as well as dimensionless (**c**) initial residual and (**d**) RMS difference between the initialized and converged solution fields for the two studied conventional FEM initialization strategies using a constant H_c value of 1 (dark grey) or by estimating H_c from an analytical proximity equation (light grey) compared to the two investigated hybrid approaches when using the pressure distribution only (light blue) or when using the pressure and film thickness distributions (dark blue) as predicted by the ANN for FEM initialization.

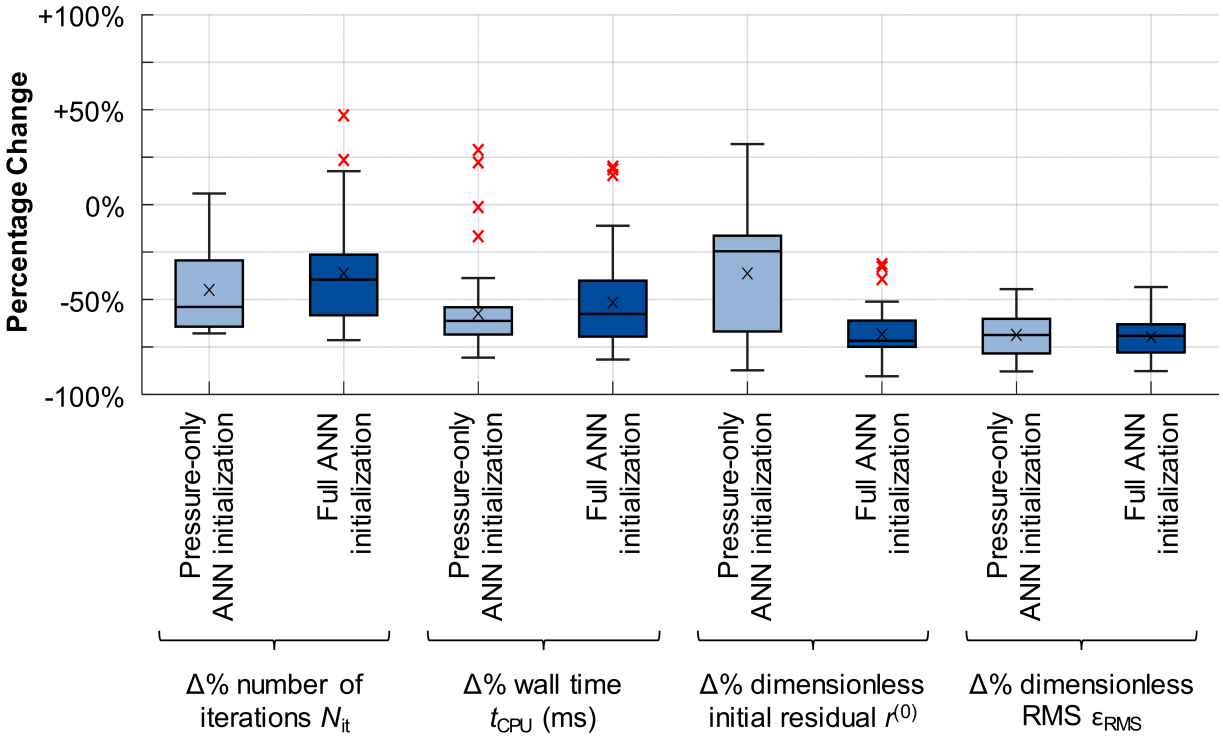


Figure 9. Percentage change in the number of iterations, overall CPU time, dimensionless initial residual and RMS difference between the initialized and converged solution fields for the studied hybrid approaches when using the pressure distribution only (light blue) or the pressure and film thickness distributions (dark blue) as predicted by the ANN for FEM initialization compared to the conventional FEM initialization by estimating H_c from an analytical proximity equation.

The dimensionless initial residuals in Figure 8c differ substantially from the trends observed for the iteration counts and overall CPU time. Among the conventional strategies, the constant FEM initialization produced a lower median initial residual than the analytical FEM initialization. This may seem surprising at first glance, given that the film thickness for the "Analytical FEM initialization" appears to be much closer to the final converged one, as compared to the "Constant FEM initialization". But in reality, for the corresponding initial solution vectors, only the rigid-body separation (a scalar quantity) is closer, while the pressure and elastic deformation fields (vector quantities) are exactly the same (i.e., Hertzian). Seemingly, a closer rigid-body separation does not necessarily produce a lower residual for the overall coupled system of equations. The analytical strategy exhibited both the highest average residual and the broadest distribution, with values extending to approximately 0.3. Thus, although the analytical film thickness equation supplies a physically informed estimate of the central film thickness, this scalar value is not necessarily consistent with the initial Hertzian pressure distribution, its corresponding elastic deformation, and the force-balance equation of the fully coupled FEM system. The pressure-only ANN initialization produced initial residuals in a range similar to that of the constant FEM initialization, but with a narrower distribution and fewer large deviations. Its median residual was markedly lower than that of the analytical FEM initialization. The full ANN initialization yielded the lowest initial residuals overall. Its median was approximately 0.03, and most values remained below approximately 0.05. The corresponding percentage changes in Figure 9 show that the full ANN initialization reduced the initial residual relative to the analytical FEM reference for every investigated operating condition. The typical reduction was approximately 60–80%. The pressure-only strategy also reduced the residual in most cases, but its distribution was considerably broader. While substantial reductions were obtained

for many conditions, a small number of cases showed residuals similar to or slightly greater than those of the analytical reference.

For the dimensionless RMS difference between the initial and converged solution distributions shown in Figure 8d, both conventional initialization strategies exhibited substantially larger RMS differences than the hybrid approaches. The constant FEM initialization showed a median of approximately 0.045–0.050. The analytical initialization had a somewhat lower median, but its distribution was broader and extended to values close to 0.1. This indicates that the analytical film thickness estimate improves the geometric proximity of the initial solution in many cases, even though this benefit was not accompanied by a lower initial residual or a consistent reduction in iteration count. The two hybrid strategies achieved very similar RMS differences. Their median values were close to 0.01, and most cases remained below approximately 0.02. Relative to the analytical FEM initialization, Figure 9 reveals typical reductions of approximately 65–85% for both approaches. The distributions of the pressure-only and full ANN strategies almost completely overlap.

4. Discussion

Taken together, the results demonstrate that the usefulness of an initial guess cannot be inferred from a single quality metric. The analytical FEM initialization often placed the initial distributions geometrically closer to the converged solution than the constant initialization, but it simultaneously produced the largest and most widely scattered initial residuals and did not reduce the typical iteration count and overall CPU time. This apparent discrepancy is consistent with the different information represented by the metrics. The RMS difference measures the overall distance between fields, whereas the residual measures whether pressure, film thickness, elastic deformation, and force balance form a mutually consistent state of the discretized nonlinear system. A scalar film thickness estimate may therefore improve the average field distance while creating an unfavorable combination with the Hertzian pressure and initially assumed deformation. For a fully coupled EHL formulation, consistency among the coupled variables is consequently more relevant than the accuracy of an isolated scalar estimate (this might be different for iterative solvers). Notably, the full ANN initialization achieved the lowest initial residual, yet the pressure-only ANN initialization produced the lowest median iteration count, while both yielded similar overall CPU times. This finding shows that a smaller initial residual does not necessarily imply the shortest nonlinear convergence path. In the pressure-only strategy, the FEM formulation reconstructed the film thickness and deformation from the ANN-informed pressure and a scalar separation estimate, thereby allowing the coupled solver to establish internal consistency during the first updates. By contrast, the full ANN strategy prescribed both local fields simultaneously. Small ANN approximation errors, interpolation errors between the ANN and FEM grids, or local physical incompatibilities between the predicted pressure and film thickness distributions can then require additional coupled corrections, even when the global initial residual is comparatively smaller. This did not result, however, in any notable differences in overall CPU times. The broader distribution and occasional increase in iteration count for the full ANN initialization suggest that supplying more predicted information is not automatically advantageous when the predicted variables are strongly coupled and not constrained by the governing equations during training. From a practical perspective, the pressure distribution appears to contain most of the information required to accelerate the present isothermal line-contact solver. The nearly identical RMS differences and overall CPU times of the two hybrid approaches, combined with the lower median iteration count of the pressure-only strategy, indicate that explicitly transferring the ANN-predicted film thickness distribution provides little additional benefit under the investigated conditions. A pressure-only coupling is also simpler because it reduces

the number of transferred fields and avoids imposing a potentially inconsistent initial deformation state. In addition, it only requires a relatively minor additional numerical effort for computing the corresponding elastic deformation field from the solution of the linear elasticity equations, used in initializing $U_Z(X)$ (see Figure 5). Nevertheless, the lower residual of the full ANN initialization may become beneficial for other nonlinear algorithms, convergence controls, or more complex models in which the initial film thickness has a stronger influence on solver robustness. The preferred initialization strategy should therefore be evaluated for the specific application rather than selected solely from surrogate-model accuracy. These findings complement previous investigations of machine-learning-assisted initialization in other numerical disciplines [24–26]. While earlier studies have primarily demonstrated the acceleration potential of learned initial guesses, the present results highlight that a more accurate or complete approximation of the solution fields does not necessarily translate into faster nonlinear convergence. In particular, the consistency among initialized variables and their interaction with the coupled governing equations appear to be decisive, motivating more selective approaches to ANN-assisted initialization.

An additional possibility for improving the initialization is to train the ANN to directly predict the rigid-body separation H_0, as demonstrated in a different hybrid TEHL framework by Kaliafetis et al. [29]. Such an approach could avoid the indirect estimation currently employed and potentially improve the consistency and convergence behavior of the initialized fields. Its effectiveness in the present fully coupled FEM formulation remains to be investigated.

Furthermore, it should be mentioned that the effectiveness of ANN-supported initialization is inherently linked to the predictive accuracy of the underlying ANN. Preliminary investigations indicated that substantial convergence improvements were primarily obtained for operating conditions where the ANN provided sufficiently accurate pressure and film thickness predictions, generally within its training domain. Outside these regions, the convergence benefits diminished or disappeared. This is consistent with the applicability limitations identified by Kelley et al. [23], who observed reduced prediction accuracy in certain regions near the training-data boundaries. Consequently, the acceleration demonstrated in the present study should not be assumed to extend beyond the ANN's established applicability range.

In this context, the practical viability of the proposed hybrid framework also depends on the offline computational effort required for ANN development. However, the intended application is not to generate a new training dataset for each engineering problem, but rather to reuse an established ANN across numerous simulations and potentially different organizations. The present study illustrates this concept by repurposing the numerical database and ANN architecture originally developed by Kelley et al. [23] for locally resolved EHL prediction. Consequently, the original computational investment can support multiple applications beyond its initial purpose. In the longer term, collaboratively developed numerical databases, FAIR data practices [39–41], and shared pretrained models could further reduce the individual development effort and facilitate broader adoption.

5. Summary and Conclusions

This study investigated a hybrid ANN–FEM approach in which locally resolved neural-network predictions were used to initialize a fully coupled FEM solver for smooth isothermal Newtonian EHL line contacts. Four initialization strategies were compared across 58 previously unseen operating conditions during ANN training using as performance metrics the required nonlinear iteration count, the overall CPU time, the dimensionless initial residual, and the dimensionless RMS difference between the initialized and converged solution fields. Both ANN-supported strategies placed the solver substantially closer to the converged

solution than the conventional initializations and generally reduced the required number of nonlinear iterations and overall CPU time. The pressure-only ANN initialization provided the greatest acceleration, with a median iteration reduction of approximately 55% and a median overall CPU time reduction of 61%, relative to the analytical FEM initialization. Full ANN initialization achieved the lowest initial residual, but its median iteration reduction was smaller, at approximately 40%, and individual cases required more iterations than conventional approaches. Its overall CPU time reduction was also smaller, at approximately 58%. Thus, supplying both predicted pressure and film thickness fields did not yield an additional convergence benefit under the investigated conditions. The results show that the quality of an initial guess cannot be assessed from field proximity or residual alone. For the present fully coupled solver, the ANN-predicted pressure distribution contained most of the information required for effective acceleration, while the FEM formulation could reconstruct the remaining coupled variables consistently. The proposed pressure-only hybrid approach therefore retains the physical consistency and accuracy of the converged numerical solution while reducing the computational effort. Future work should examine its transferability to broader parameter ranges and to non-Newtonian, thermal, transient, and multidimensional EHL models.

Author Contributions: Conceptualization, J.K., W.H. and M.M.; Methodology, J.K., W.H. and M.M.; Software, J.K.; Validation, J.K. and W.H.; Formal Analysis, J.K., W.H. and M.M.; Investigation, J.K.; Resources, M.M.; Data Curation, J.K., W.H. and M.M.; Writing—Original Draft Preparation, J.K. and M.M.; Writing—Review and Editing, J.K., W.H., V.S., M.T., C.Z., T.L. and M.M.; Visualization, J.K. and M.M.; Supervision, W.H. and M.M.; Funding Acquisition, W.H., T.L. and M.M. All authors have read and agreed to the published version of the manuscript.

Funding: J.K. and M.M. acknowledge the financial support from Leibniz University Hannover, the Lower Saxony Ministry of Science and Culture (MWK), and Volkswagen Foundation within the Zukunft.Niedersachsen Lower Saxony Profile Professorship. W.H., T.L., and M.M. thank the German Research Foundation (DFG) for funding the research project "AI-Driven Modelling of Atypical TEHL Contacts in Worm Gears and Tapered Roller Bearings (AIM@TEHL)" (587733490).

Data Availability Statement: The data supporting the findings reported in this study are available from the corresponding authors upon reasonable request.

Conflicts of Interest: The authors declare no conflict of interest.

Appendix A

Table A1. Parameter variations considered in the benchmarking study.

Nr.	L [-]	M [-]	R [m]	u_{ent} [m/s]	F_N [N/m]	p_H [MPa]
1	3	25	0.012	0.0085	50,400	384
2	3	25	0.013	0.0092	54,600	384
3	3	25	0.014	0.0099	58,800	384
4	3	25	0.015	0.0106	63,000	384
5	4	25	0.007	0.0157	52,200	512
6	4	25	0.008	0.0179	59,700	512
7	4	25	0.009	0.0202	67,200	512
8	4	25	0.010	0.0224	74,600	512
9	4	25	0.011	0.0246	82,100	512

Table A1. *Cont.*

Nr.	L [-]	M [-]	R [m]	u_{ent} [m/s]	F_N [N/m]	p_H [MPa]
10	4	25	0.012	0.0269	89,600	512
11	4	25	0.013	0.0291	97,000	512
12	4	25	0.014	0.0314	104,500	512
13	4	25	0.015	0.0336	111,900	512
14	5	10	0.011	0.0602	51,300	405
15	5	10	0.012	0.0656	56,000	405
16	5	10	0.013	0.0711	60,600	405
17	5	10	0.014	0.0766	65,300	405
18	5	10	0.015	0.082	70,000	405
19	5	25	0.005	0.0273	58,300	640
20	5	25	0.006	0.0328	70,000	640
21	5	25	0.007	0.0383	81,600	640
22	5	25	0.008	0.0437	93,300	640
23	5	25	0.009	0.0492	104,900	640
24	5	25	0.010	0.0547	116,600	640
25	5	25	0.011	0.0602	128,300	640
26	5	25	0.012	0.0656	139,900	640
27	6	5	0.015	0.1701	50,400	344
28	6	10	0.008	0.0907	53,700	486
29	6	10	0.009	0.1021	60,400	486
30	6	10	0.010	0.1134	67,200	486
31	6	10	0.011	0.1247	73,900	486
32	6	10	0.012	0.1361	80,600	486
33	6	10	0.013	0.1474	87,300	486
34	6	10	0.014	0.1588	94,000	486
35	6	10	0.015	0.1701	100,700	486
36	6	25	0.004	0.0454	67,200	769
37	6	25	0.005	0.0567	84,000	769
38	6	25	0.006	0.068	100,700	769
39	6	25	0.007	0.0794	117,500	769
40	6	25	0.008	0.0907	134,300	769
41	7	5	0.011	0.2311	50,300	401
42	7	10	0.006	0.1261	54,900	567
43	7	10	0.007	0.1471	64,000	567
44	7	10	0.008	0.1681	73,100	567
45	7	10	0.009	0.1891	82,300	567
46	7	10	0.010	0.2101	91,400	567

Table A1. *Cont.*

Nr.	L [-]	M [-]	R [m]	u_{ent} [m/s]	F_N [N/m]	p_H [MPa]
47	7	10	0.011	0.2311	100,600	567
48	7	25	0.004	0.084	91,400	897
49	7	25	0.005	0.105	114,300	897
50	7	25	0.006	0.1261	137,100	897
51	8	10	0.005	0.1792	59,700	648
52	8	10	0.006	0.215	71,600	648
53	8	25	0.002	0.0717	59,700	1025
54	8	25	0.004	0.1434	119,400	1025
55	8	25	0.005	0.1792	149,300	1025
56	9	10	0.004	0.2296	60,400	729
57	9	25	0.002	0.1148	75,600	1153
58	10	25	0.002	0.175	93,300	1281

References

1. Dowson, D.; Higginson, G.R. A numerical solution to the elasto-hydrodynamic problem. *J. Mech. Eng. Sci.* **1959**, *1*, 6–15. [CrossRef]
2. Venner, C.H.; Napel, W. Multilevel solution of the elastohydrodynamically lubricated circular contact problem Part I: Theory and numerical algorithm. *Wear* **1992**, *152*, 351–367. [CrossRef]
3. Venner, C.H.; Napel, W. Multilevel solution of the elastohydrodynamically lubricated circular contact problem part 2: Smooth surface results. *Wear* **1992**, *152*, 369–381. [CrossRef]
4. Kaliafetis, F.; Dini, D.; Ewen, J.P.; Ardah, S. A Finite Volume-Based Unified Transient Deterministic Framework for Lubrication Modelling. *Lubricants* **2026**, *14*, 281. [CrossRef]
5. Ardah, S.; Profito, F.J.; Dini, D. An integrated finite volume framework for thermal elasto-hydrodynamic lubrication. *Tribol. Int.* **2023**, *177*, 107935. [CrossRef]
6. Hajishafiee, A.; Kadiric, A.; Ioannides, S.; Dini, D. A coupled finite-volume CFD solver for two-dimensional elasto-hydrodynamic lubrication problems with particular application to rolling element bearings. *Tribol. Int.* **2017**, *109*, 258–273. [CrossRef]
7. Habchi, W. *Finite Element Modeling of Elastohydrodynamic Lubrication Problems*; John Wiley & Sons Incorporated: Newark, NI, USA, 2018.
8. Pastewka, L.; Vakis, A.I.; Eder, S.J.; Aghababaei, R.; Almqvist, A.; Carbone, G.; Chandross, M.; Dini, D.; Ehrich, H.J.; Ewen, J.P.; et al. Modeling in tribology: Recent advances, applications, and open questions. *Tribol. Int.* **2026**, *218*, 111326. [CrossRef]
9. Habchi, W.; Issa, J.S. An Exact and General Model Order Reduction Technique for the Finite Element Solution of Elastohydrodynamic Lubrication Problems. *J. Tribol.* **2017**, *139*, 51501. [CrossRef]
10. Marian, M.; Bartz, M.; Wartzack, S.; Rosenkranz, A. Non-Dimensional Groups, Film Thickness Equations and Correction Factors for Elastohydrodynamic Lubrication: A Review. *Lubricants* **2020**, *8*, 95. [CrossRef]
11. Paturi, U.M.R.; Palakurthy, S.T.; Reddy, N.S. The Role of Machine Learning in Tribology: A Systematic Review. *Arch. Comput. Methods Eng.* **2023**, *30*, 1345–1397. [CrossRef]
12. Sose, A.T.; Joshi, S.Y.; Kunche, L.K.; Wang, F.; Deshmukh, S.A. A review of recent advances and applications of machine learning in tribology. *Phys. Chem. Chem. Phys.* **2023**, *25*, 4408–4443. [CrossRef] [PubMed]
13. Yin, N.; Yang, P.; Liu, S.; Pan, S.; Zhang, Z. AI for tribology: Present and future. *Friction* **2024**, *12*, 1060–1097. [CrossRef]
14. Shah, R.; Jaramillo, R.; Thomas, G.; Rayhan, T.; Hossain, N.; Kchaou, M.; Profito, F.J.; Rosenkranz, A. Artificial Intelligence and Machine Learning in Tribology: Selected Case Studies and Overall Potential. *Adv. Eng. Mater.* **2025**, *27*, 2401944. [CrossRef]
15. Marian, M.; Mursak, J.; Bartz, M.; Profito, F.J.; Rosenkranz, A.; Wartzack, S. Predicting EHL film thickness parameters by machine learning approaches. *Friction* **2022**, *11*, 992–1013. [CrossRef]
16. Issa, J.; El Hajj, A.; Vergne, P.; Habchi, W. Machine Learning for Film Thickness Prediction in Elastohydrodynamic Lubricated Elliptical Contacts. *Lubricants* **2023**, *11*, 497. [CrossRef]
17. Tošić, M.; Marian, M.; Habchi, W.; Lohner, T.; Stahl, K. Application of machine learning for film thickness prediction in elliptical EHL contact with varying entrainment angle. *Tribol. Int.* **2024**, *199*, 109940. [CrossRef]

18. Habchi, W.; Bair, S. Machine-Learning-Assisted Identification and Formulation of High-Pressure Lubricant-Piezoviscous-Response Parameters for Minimum Film Thickness Determination in Elastohydrodynamic Circular Contacts. *Tribol. Lett.* **2024**, *72*, 134. [CrossRef]
19. Zhang, C.; Tošić, M.; Kelley, J.; Habchi, W.; Marian, M.; Lohner, T. A modular and generalized machine learning approach for non-Newtonian EHL film thickness prediction. *Tribol. Int.* **2026**, *225*, 112211. [CrossRef]
20. Walker, J.; Questa, H.; Raman, A.; Ahmed, M.; Mohammadpour, M.; Bewsher, S.R.; Offner, G. Application of Tribological Artificial Neural Networks in Machine Elements. *Tribol. Lett.* **2023**, *71*, 3. [CrossRef]
21. Wang, L.; Zhao, N.; An, X.; Li, J. Application of artificial neural networks for predicting friction coefficient and film thickness considering non-Newtonian and thermal effects. *J. Supercomput* **2025**, *81*, 876. [CrossRef]
22. Cartwright, S.; Rothwell, B.C.; Figueredo, G.; Medina, H.; Eastwick, C.; Layton, J.; Ambrose, S. A machine learning-driven approach to predicting thermo-elasto-hydrodynamic lubrication in journal bearings. *Tribol. Int.* **2024**, *196*, 109670. [CrossRef]
23. Kelley, J.; Schneider, V.; Poll, G.; Marian, M. Enhancing practical modeling: A neural network approach for locally-resolved prediction of elastohydrodynamic line contacts. *Tribol. Int.* **2024**, *199*, 109988. [CrossRef]
24. Aghili, J.; Franck, E.; Hild, R.; Michel-Dansac, V.; Vigon, V. Accelerating the convergence of Newton's method for nonlinear elliptic PDEs using Fourier neural operators. *Commun. Nonlinear Sci. Numer. Simul.* **2025**, *140*, 108434. [CrossRef]
25. Zhou, X.-H.; Han, J.; Zafar, M.I.; Wolf, E.M.; Schrock, C.R.; Roy, C.J.; Xiao, H. Neural operator-based super-fidelity: A warm-start approach for accelerating steady-state simulations. *J. Comput. Phys.* **2025**, *529*, 113871. [CrossRef]
26. Taghikhani, K.; Yamazaki, Y.; Varghese, J.P.; Apel, M.; Asl, R.N.; Rezaei, S. Neural-Initialized Newton: Accelerating Nonlinear Finite Elements via Operator Learning. *Int. J. Numer. Meth. Engng.* **2026**, *127*, e70380. [CrossRef]
27. Eshaghi, M.S.; Anitescu, C.; Valizadeh, N.; Wang, Y.; Zhuang, X.; Rabczuk, T. NOWS: Neural Operator Warm Starts for accelerating iterative solvers. *Comput. Methods Appl. Mech. Eng.* **2026**, *458*, 118989. [CrossRef]
28. Wang, Y.; Hao, Z.; Eshaghi, M.S.; Anitescu, C.; Zhuang, X.; Rabczuk, T.; Liu, Y. Pretrain finite element method: A pretraining and warm-start framework for PDEs via physics-informed neural operators. *J. Mech. Phys. Solids* **2026**, *214*, 106682. [CrossRef]
29. Kaliafetis, F.; Ardah, S.; Ewen, J.P.; Dini, D. Using artificial neural networks to accelerate thermo-elastohydrodynamic lubrication simulations. *Tribol. Int.* **2025**, *212*, 110978. [CrossRef]
30. Roelands, C. Correlational Aspects of the Viscosity-Temperature-Pressure Relationship of Lubricating Oils. Ph.D. Thesis, Delft University of Technology, Delft, The Netherlands, 1966.
31. Dowson, D.; Higginson, G.R. *Elasto-Hydrodynamic Lubrication*, SI ed.; Pergamon Press: Oxford, UK, 1977.
32. Dowson, D.; Higginson, G.R. The Effect of Material Properties on the Lubrication of Elastic Rollers. *Arch. J. Mech. Eng. Sci.* **1960**, *2*, 188–194. [CrossRef]
33. Dowson, D.; Higginson, G.R.; Whitaker, A.V. Elasto-hydrodynamic lubrication: A survey of isothermal solutions. *J. Mech. Eng. Sci.* **1962**, *4*, 121–126. [CrossRef]
34. Moes, H. Discussion on Paper D1 by D. Dowson. *Proc. Instn. Mech. Engrs.* **1966**, *180*, 244–245.
35. Moes, H. Communications. In *Proceedings of the Symposium on Elastohydrodynamic Lubrication*; Institution of Mechanical Engineers: London, UK, 1965; pp. 244–245.
36. Habchi, W.; Demirci, I.; Eyheramendy, D.; Morales-Espejel, G.; Vergne, P. A finite element approach of thin film lubrication in circular EHD contacts. *Tribol. Int.* **2007**, *40*, 1466–1473. [CrossRef]
37. Davis, T.A.; Duff, I.S. An Unsymmetric-Pattern Multifrontal Method for Sparse LU Factorization. *SIAM J. Matrix Anal. Appl.* **1997**, *18*, 140–158. [CrossRef]
38. Pan, P.; Hamrock, B.J. Simple Formulas for Performance Parameters Used in Elastohydrodynamically Lubricated Line Contacts. *J. Tribol. Trans. ASME* **1989**, *111*, 246–251. [CrossRef]
39. Garabedian, N.; Tysoe, W.T. From Data Islands to Knowledge Networks in Tribology: Understanding the Modern Data Architecture. *Tribol. Lett.* **2026**, *74*, 86. [CrossRef]
40. Garabedian, N.T.; Schreiber, P.J.; Brandt, N.; Zschumme, P.; Blatter, I.L.; Dollmann, A.; Haug, C.; Kümmel, D.; Li, Y.; Meyer, F.; et al. Generating FAIR research data in experimental tribology. *Sci. Data* **2022**, *9*, 315. [CrossRef]
41. Brandt, N.; Garabedian, N.T.; Schoof, E.; Schreiber, P.J.; Zschumme, P.; Greiner, C.; Selzer, M. Managing FAIR Tribological Data Using Kadi4Mat. *Data* **2022**, *7*, 15. [CrossRef]

Disclaimer/Publisher's Note: The statements, opinions and data contained in all publications are solely those of the individual author(s) and contributor(s) and not of MDPI and/or the editor(s). MDPI and/or the editor(s) disclaim responsibility for any injury to people or property resulting from any ideas, methods, instructions or products referred to in the content.